UC Irvine
UC Irvine Previously Published Works

Title
Biospheric primary production during an ENSO transition.

Permalink
https://escholarship.org/uc/item/51z7z4n6

Journal
Science (New York, N.Y.), 291(5513)

ISSN
0036-8075

Authors
Behrenfeld, MJ
Randerson, JT
McClain, CR
et al.

Publication Date
2001-03-01

DOI
10.1126/science.1055071

Copyright Information
This work is made available under the terms of a Creative Commons Attribution License, availalbe at https://creativecommons.org/licenses/by/4.0/

Peer reviewed

eScholarship.org Powered by the California Digital Library
University of California

cause the area of the Antarctic "ozone hole" to spread beyond those measured in the 1990s. Thus, the effect of denitrification on ozone recovery in both hemispheres cannot be ignored and must be included quantitatively in assessment models for better predictions of future springtime polar ozone trends.

References and Notes

1. J. L. Stanford, J. S. Davis, *Bull. Am. Meteorol. Soc.* **55**, 213 (1974).
2. J. C. Farman, B. G. Gardiner, J. D. Shanklin, *Nature* **315**, 207 (1985).
3. M. J. Molina, F. S. Rowland, *Nature* **249**, 820 (1974).
4. S. Solomon, R. R. Garcia, F. S. Rowland, D. J. Wuebbles, *Nature* **321**, 755 (1986).
5. M. J. Molina, T-L. Tso, L. T. Molina, F. C. Y. Wang, *Science* **238**, 1253 (1987).
6. M. A. Tolbert, M. J. Rossi, R. Malhotra, D. M. Golden, *Science* **238**, 1258 (1987).
7. O. B. Toon, P. Hamill, R. P. Turco, J. Pinto, *Geophys. Res. Lett.* **13,** 1284 (1986).
8. P. J. Crutzen, F. Arnold, *Nature* **324**, 651 (1986).
9. A. Tabazadeh *et al.*, *Science* **288**, 1407 (2000).
10. R. J. Salawitch, G. P. Gobbi, S. C. Wofsy, M. B. McElroy, *Nature* **339**, 525 (1989).
11. O. B. Toon, R. P. Turco, P. Hamill, *Geophys. Res. Lett.* **17**, 445 (1990).
12. M. L. Santee, G. L. Manney, L. Froidevaux, W. G. Read, J. Waters, *J. Geophys. Res.* **104**, 8225 (1999).
13. *WMO Scientific Assessment of Ozone Depletion: 1998, Rep. 44* (1999), chapter 3.
14. Selective nucleation of just a few STS particles into more stable crystalline forms of nitric acid sets the stage for the differential growth process (*10*, *11*), which results in the occurrence of a very small population of relatively large nitric acid hydrate cloud particles. It is the sedimentation of these large nitric acid hydrate particles that leads to denitrification.
15. M. A. Tolbert, *Science* **272**, 1597 (1996).
16. O. B. Toon, A. Tabazadeh, E. V. Browell, J. Jordan, *J. Geophys. Res.* **105**, 20589, (2000).
17. A. Tabazadeh, R. P. Turco, K. Drdla, M. Z. Jacobson, O. B. Toon, *Geophy. Res. Lett.* **21**, 1619 (1994).
18. K. S. Carslaw, B. P. Luo, S. L. Clegg, T. Peter, P. Brimblecombe, P. Crutzen, *Geophys. Res. Lett.* **21**, 2479 (1994).
19. A. K. Bertram, D. B. Dickens, J. J. Sloan, *J. Geophys. Res.* **105**, 9283 (2000).
20. D. Salcedo, L. T. Molina, M. J. Molina, *J. Phys. Chem.* **105**, 1433 (2001).
21. The results of laboratory freezing rates are parameterized into simple functions of the form (*20*)

$$J_{\mathrm{NAD}} = 1.138 \times 10^{34}\sqrt{T}r^3 \exp\left[\frac{-\Delta G_{\mathrm{act}}^{\mathrm{NAD}}}{RT}\right],$$

where

$$\Delta G_{\mathrm{act}}^{\mathrm{NAD}} = (28.8 \pm 0.2) - (0.37 \pm 0.01)S_{\mathrm{NAD}}$$

$$J_{\mathrm{NAT}} = 9.269 \times 10^{33}\sqrt{T}r^3 \exp\left[\frac{-\Delta G_{\mathrm{act}}^{\mathrm{NAT}}}{RT}\right],$$

where

$$\Delta G_{\mathrm{act}}^{\mathrm{NAT}} = (30.9 \pm 0.3) - (0.14 \pm 0.0004)S_{\mathrm{NAT}}$$

where J is the freezing rate of a single particle in sec^{-1}, T is temperature in K, r is the particle radius in cm, ΔG_{act} is the activation free energy for the formation of hydrate germs in solution in units of kcal mol^{-1} (*20*), S is hydrate saturation in solution, and R is the universal ideal gas constant in units of kcal $\mathrm{mol}^{-1}\ \mathrm{K}^{-1}$. To account for the effect of particle size on freezing, we have slightly modified (*35*) the pre-exponential factor from that given in Salcedo *et al.* (*20*).
22. The 1D model uses vertical temperature profiles that are constructed using the archived NASA Goddard National Centers for Environmental Prediction (NCEP) data (*36*). To obtain a vertical temperature profile, a single position is first selected on the 450 K surface (~50 mbar) inside a cloudy region ($T < 192$ K). Next, air parcel trajectories (*36*) are run forward and backward for 2 weeks from the chosen location to obtain a 4-week-long temperature and position history of an air parcel. Positions along the 4-week-long trajectory at the 450 K level are used to read off vertical temperature profiles at each location and time along the parcel's path using the NCEP data.
23. E. J. Jensen, O. B. Toon, D. L. Westphal, S. Kinne, A. J. Heymsfield, *J. Geophys. Res.* **99**, 10443 (1994).
24. Cloud model sensitivity studies (*22*) indicate that hourly NAD and/or NAT hydrate particle production rates $<\sim 10^{-5}\ \mathrm{cm}^{-3}$ (Fig. 1) can result in 10% denitrification at most in typical air parcels before particle evaporation occurs. Thus, NAD particle production within the nucleation window is the dominant process that controls the overall atmospheric number density of the nitric acid hydrated particles. Direct NAT particle production rate from STS is $<10^{-5}\ \mathrm{cm}^{-3}$ in the atmosphere (Fig. 1), making this process unimportant to denitrification. The temperature margins of the nucleation window vary as a function of total pressure, H_2O mixing ratio, and HNO_3 mixing ratio.
25. To compute cloud microphysical properties, 20 initial points were homogeneously distributed within the 192 K temperature contour at 50 mbar for the 3 days marked as dashed lines in Fig. 2. These days represent cloudy conditions in the middle of each study period (marked as bounded arrows in Fig. 2). We ran trajectories forward and backward from each initialized point to obtain 20 4-week-long air parcel temperature histories for each winter; their corresponding vertical temperature profiles are constructed as described above (*22*).
26. D. W. Fahey *et al.*, *Science* **291**, 1026 (2001).
27. For standard model runs, mean ΔG values were used in the J expressions for both NAD and NAT (*21*). Sensitivity studies were also performed by using upper and lower limits for ΔG in the J expressions for both hydrates.
28. To account for NAD to NAT conversion in the model, the assumptions were used for J values as follows: J_{NAT} = standard J_{NAD} + standard J_{NAT} and $J_{\mathrm{NAD}} = 0$ (*27*). Most laboratory observations indicate that the metastable NAD phase is the nucleus that initially forms in aerosol particles (*13*, *19*, *20*, *37*). In general, kinetically favorable phases usually nucleate first in particles, and in time such metastable phases often but not always transition into the most stable form (*37*). Thus, the possibility of NAD to NAT conversion in the atmosphere is likely, and recent in situ NAT particle observations (*38*) seem to support this hypothesis.
29. Due to cold temperatures roughly 1 to 4 ppbv of HNO_3 between 17 to 23 km is sequestered in the STS phase at the end of the Antarctic calculations in most air parcels. The STS content is sensitive to both J uncertainties (*27*) and the assumption of NAD to NAT conversion (*28*).
30. G. L. Manney, J. L. Sabutis, *Geophys. Res. Lett.* **27**, 2589 (2000).
31. M. L. Santee, G. L. Manney, N. J. Livesey, J. W. Waters, *Geophys. Res. Lett.* **27**, 3213 (2000).
32. Y. Kondo, H. Irie, M. Koike, G. E. Bodeker, *Geophys. Res. Lett.* **27**, 337 (2000).
33. H. J. Hintsa, *Geophys. Res. Lett.,* **25**, 501 (1998).
34. D. T. Shindell, D. Rind, P. Lonergan, *Nature*, **392**, 589 (1998).
35. A. Tabazadeh, S. T. Martin, J. S. Lin, *Geophys. Res. Lett.* **27**, 1111 (2000).
36. M. R. Schoeberl, S. Doiron, L. R. Lait, P. A. Newman, A. J. Krueger, *J. Geophys. Res.* **98**, 2949 (1992).
37. D. R. Worsnop, L. E. Fox, M. S. Zahniser, S. C. Wofsy, *Science* **259**, 71 (1993).
38. C. Voigt *et al.*, *Science* **290**, 1756 (2000).
39. D. R. Hanson, K. Mauersberger, *Geophys. Res. Lett.* **15**, 855 (1988).
40. J. E. Dye *et al.*, *J. Geophys. Res.* **97**, 8015 (1992).

41. We are grateful to D. Salcedo for providing us with preprint copies of her paper and thesis on stratospheric aerosol freezing. We thank M. Santee, N. Larsen, P. Hamill, and A. Ackerman for helpful comments and suggestions. Supported by two separate NASA programs, the Upper Atmosphere Research Satellite (UARS) and the Atmospheric Chemistry Modeling and Analysis Program (ACMAP). A.T. also acknowledges support from a Presidential Early Career Award for Scientists and Engineers.

7 November 2000; accepted 28 February 2001

Biospheric Primary Production During an ENSO Transition

Michael J. Behrenfeld,[1]* James T. Randerson,[2] Charles R. McClain,[1] Gene C. Feldman,[1] Sietse O. Los,[3] Compton J. Tucker,[1] Paul G. Falkowski,[4] Christopher B. Field,[5] Robert Frouin,[6] Wayne E. Esaias,[1] Dorota D. Kolber,[4] Nathan H. Pollack[7]

The Sea-viewing Wide Field-of-view Sensor (SeaWiFS) provides global monthly measurements of both oceanic phytoplankton chlorophyll biomass and light harvesting by land plants. These measurements allowed the comparison of simultaneous ocean and land net primary production (NPP) responses to a major El Niño to La Niña transition. Between September 1997 and August 2000, biospheric NPP varied by 6 petagrams of carbon per year (from 111 to 117 petagrams of carbon per year). Increases in ocean NPP were pronounced in tropical regions where El Niño–Southern Oscillation (ENSO) impacts on upwelling and nutrient availability were greatest. Globally, land NPP did not exhibit a clear ENSO response, although regional changes were substantial.

Temporal changes in the physical environment are manifested in the light-harvesting capacity of plant communities throughout the biosphere and can be monitored remotely by changes in surface chlorophyll concentration (C_{sat}) in the oceans and the Normalized Difference Vegetation Index (NDVI) on land. A continuous, 20-year global record of satellite NDVI has permitted characterization of interannual, climate-driven changes in terrestrial photosynthesis (*1–5*). Coincident changes in ocean productivity have not been assessed because an analogous long-term global C_{sat} record does not exist. The first C_{sat} measure-

ments were made with the Coastal Zone Color Scanner (CZCS: 1978–86), but this proof-of-concept sensor collected data on a highly irregular basis that yielded incomplete global coverage even after integration over the entire 8-year mission. Eleven years later, SeaWiFS was launched, marking the beginning of the first multiyear satellite measurements of phytoplankton biomass since CZCS. SeaWiFS now provides greater global coverage of C_{sat} each month than was achieved throughout the lifetime of CZCS. In addition, SeaWiFS is the first satellite instrument with the spectral coverage and dynamic range necessary to derive both C_{sat} and NDVI. Here we report spatial and temporal changes in the photosynthetic biosphere for an El Niño to La Niña transition period, as recorded during the first 3 years of the SeaWiFS mission.

We analyzed global, 4-km resolution, monthly SeaWiFS C_{sat} and NDVI data collected between September 1997 and August 2000. Stability of the sensor was characterized from monthly lunar-based calibrations and derived products verified by comparison with field measurements (*6–8*). Biospheric net primary production (NPP) was estimated following the approach of Field *et al.* (*9*), which integrates the Vertically Generalized Production Model (VGPM) for the oceans (*10*) with the Carnegie-Ames-Stanford Approach (CASA) for land (*11*, *12*). Variations in NPP for the CASA-VGPM model arise from changes in three factors: (i) incident photosynthetically active radiation (PAR), (ii) the fraction of radiation absorbed by plants (related to C_{sat} and NDVI), and (iii) light use efficiency (ε). Coincident changes in these factors collectively control NPP. Unlike previous calculations that used C_{sat}, NDVI, and climate data from different periods (*9*), all data used in the current NPP estimates were collected during the SeaWiFS period (*13*). The CASA-VGPM model was operated on a monthly time step.

SeaWiFS measurements began near the peak of the 1997–98 El Niño event (by some measures, one of the strongest on record) (*14*) and then continued through an equally strong La Niña period. A pronounced seasonal cycle dominated temporal variability in global mean C_{sat} throughout the SeaWiFS record (Fig. 1A). Summer phytoplankton blooms in the Northern Hemisphere exceeded those in the Southern Hemisphere, causing minima in global mean C_{sat} between November and March and maxima between May and September. Superimposed on this prominent seasonal cycle was a clear El Niño–Southern Oscillation (ENSO)–related change in ocean productivity, as illustrated by the monthly C_{sat} anomaly record (Fig. 1A) (*15*). The El Niño to La Niña transition altered ocean nutrient distributions, causing nearly a 10% increase in global mean C_{sat} between September 1997 and December 1998. Changes in C_{sat} during this period were not restricted to the equatorial belt but rather were global in extent. During the subsequent La Niña period of January 1999 to August 2000, C_{sat} continued to increase at the reduced rate of 2.2% per year, primarily reflecting increased phytoplankton biomass in the Pacific Ocean.

Temporal changes in ocean NPP exhibited seasonal and interannual patterns similar to C_{sat}, increasing from 54 to 59 Pg C year^{-1} (Pg = 10^{15} g) over the 3-year SeaWiFS period. Regionally, NPP was highest near equatorial and eastern margin upwelling centers, at high latitudes in the Northern Hemisphere, and within the southern subtropical convergence zone (Fig. 2, A and B). Seasonal changes in Southern Hemisphere NPP mirrored those of the Northern Hemisphere, except between 40° and 75°S latitude from October to April (Fig. 3). At >40°N, phytoplankton growth is restricted by deep mixing and low PAR during winter months and then increases markedly in the summer when surface waters rich in nutrients become stratified and PAR is high. Consequently, NPP was strongly seasonal in this region, varying from 0 to 49 g C m^{-2} month^{-1} (Fig. 3). In contrast, seasonality in NPP was greatly dampened poleward of 40°S, with summer values decreasing from 27 to 7 g C m^{-2} month^{-1} between 40° and 70°S (Fig. 3). This absence of a high-latitude, Southern Hemisphere bloom results from weak seasonality in factors limiting phytoplankton growth, particularly iron and vertical mixing (*16–19*). We calculated that a 9 Pg C year^{-1} increase in NPP would result if seasonal changes in phytoplankton biomass between 40° and 75°S paralleled those in the Northern Hemisphere (*20*).

On land, temporal changes in global mean NDVI were dominated by strong seasonal fluctuations, with minima of 0.44 ± 0.01 (dimensionless) between December and February and maxima of 0.55 ± 0.01 between June and September (Fig. 1B). Land NPP peaked between 15°S and 10°N, reaching 87 g C m^{-2} month^{-1}, and varied seasonally at >35°N from 0 to 75 g C m^{-2} month^{-1} (Fig. 2, A and B). Despite the strong El Niño and La Niña, monthly anomalies indicated little systematic impact on global mean NDVI for the 3-year SeaWiFS record (Fig. 1B) (*15*). Land NPP was nearly constant for both climate regimes, ranging from 57 to 58 Pg of C year^{-1} between September 1997 and August 2000. Substantial ENSO-related regional changes, however, are hidden in these global integrals.

Biospheric distributions of NPP register

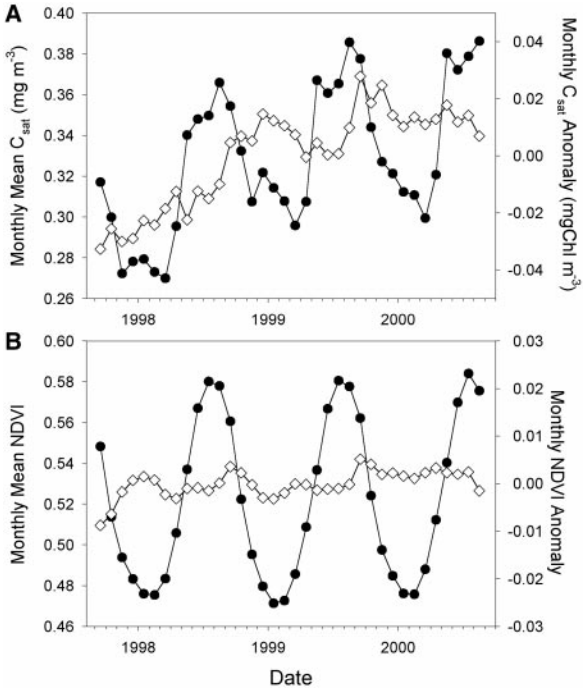

Fig. 1. Global monthly means and anomalies in (**A**) surface ocean chlorophyll (C_{sat}: mgChl m^{-3}) and (**B**) land NDVI (dimensionless) for SeaWiFS measurements between September 1997 and August 2000. Anomalies were calculated as the difference between C_{sat} or NDVI for a given month and the average value for that month during the 3-year time series. (A) ●, monthly mean C_{sat} (left axis); ◇, monthly anomaly (right axis). (B) ●, monthly mean NDVI (left axis); ◇, monthly anomaly (right axis).

[1]National Aeronautic and Space Administration, Goddard Space Flight Center, Greenbelt, MD 20771, USA. [2]California Institute of Technology, Divisions of Engineering and Applied Science and Geological and Planetary Sciences, Mail Stop 100-23, Pasadena, CA 91125, USA. [3]Department of Geography, University of Wales Swansea, Singleton Park, Swansea SA2 8PP, UK. [4]Institute of Marine and Coastal Sciences, Rutgers, State University of New Jersey, New Brunswick, NJ 08901, USA. [5]Carnegie Institution of Washington, Department of Plant Biology, 260 Panama Street, Stanford, CA 94305, USA. [6]Scripps Institution of Oceanography, 8605 La Jolla Shores Drive, La Jolla, CA 92037, USA. [7]Science Systems and Applications Incorporated, National Aeronautic and Space Administration, Goddard Space Flight Center, Greenbelt, MD 20771, USA.

*To whom correspondence should be addressed. E-mail: mjb@neptune.gsfc.nasa.gov

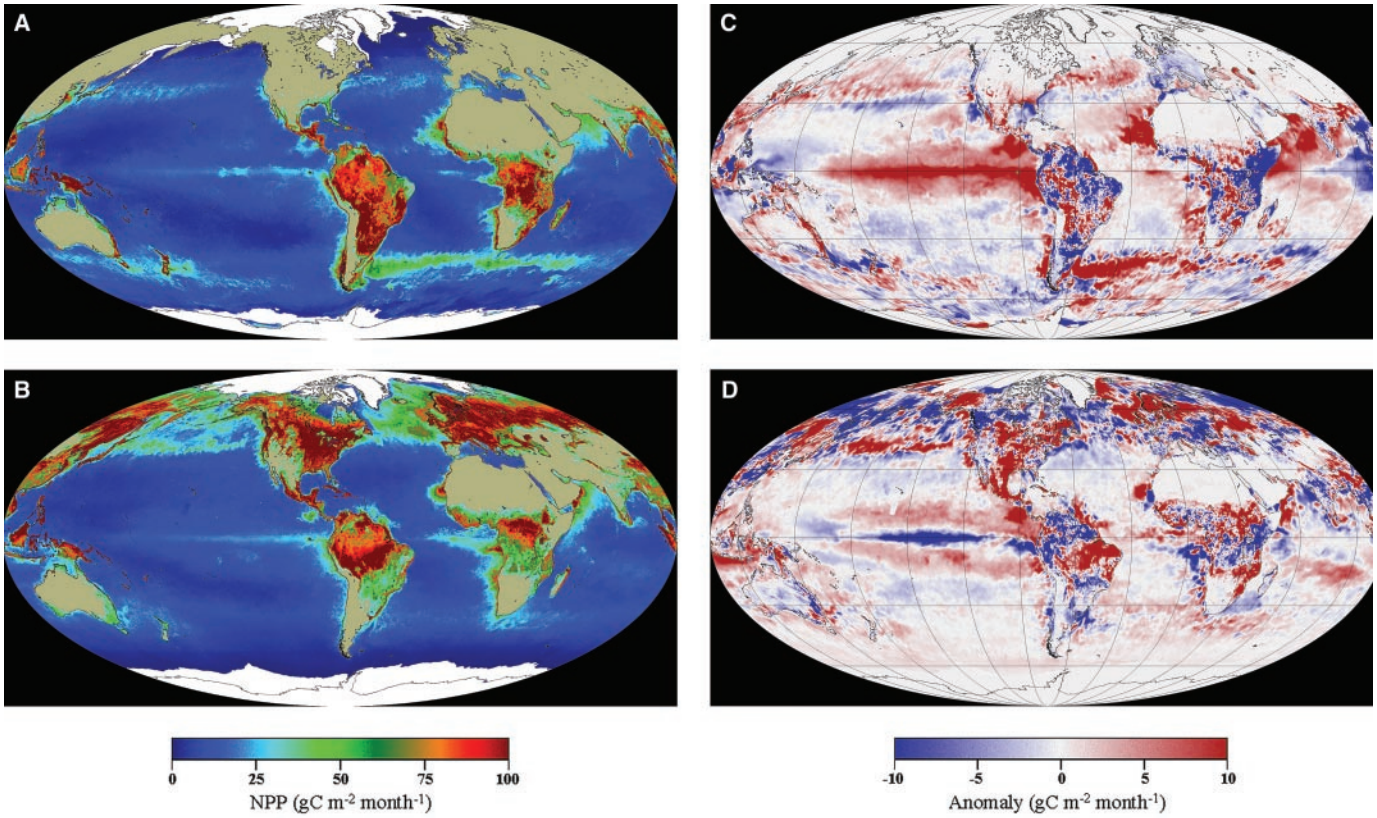

Fig. 2. Seasonal average and interannual differences in biospheric NPP (g C m^{-2} $month^{-1}$) estimated with SeaWiFS data and the integrated CASA-VGPM model (*9*). Average NPP for (**A**) the La Niña Austral summer of December 1998 to February 1999 and (**B**) the La Niña Boreal summer of June to August 1999. (A and B) White, ice cover during (A) January and (B) July; tan, near-zero NPP for terrestrial regions not permanently covered by ice. (**C**) Transition from El Niño to La Niña conditions resulted in substantial regional changes in NPP, as illustrated by interannual differences in Austral summer NPP (i.e., average NPP for December 1998 to February 1999 minus average NPP for December 1997 to February 1998). (**D**) Changes in NPP between two La Niña Boreal summers (1999 minus 1998). (C and D) Red, increase in NPP; blue, decrease in NPP; white, no substantial interannual change in NPP.

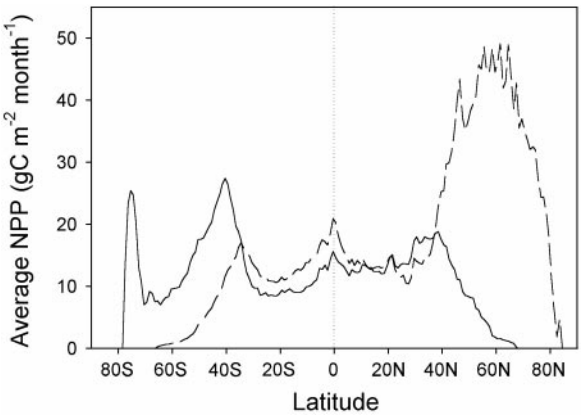

Fig. 3. Seasonal changes in the latitudinal distribution of ocean NPP (g C m^{-2} $month^{-1}$) for the 3-year SeaWiFS record. Solid line, average Austral summer (December through February) NPP; dashed line, average Boreal summer (June through August) NPP. The vertical dotted line marks the equator.

spatiotemporal variations in light, soil moisture, nutrient availability, and temperature. Interannual variability in NPP is thus linked to regional changes in physical forcings that regulate these resources and environmental conditions. Particularly striking examples of this relation during the 1997–98 El Niño to La Niña transition included an increase in equatorial Pacific NPP resulting from enhanced upwelling (*21*) and reduced terrestrial NPP in eastern Africa related to decreased precipitation (Fig. 2C). Additional features of the transition included (i) a change in Indian Ocean circulation that increased NPP in the northeast while decreasing productivity west of Indonesia (*22*), (ii) precipitation-related changes in NPP over Amazonia and Argentina, and (iii) nutrient-driven increases in ocean NPP east of Argentina and in the Mauritanian upwelling plume off western Africa (Fig. 2C). Persistent La Niña conditions between the Boreal summers of 1998 and 1999 led to spatially heterogeneous changes in NPP, including a large equatorial decrease and off-equatorial increase in the Pacific Ocean that likely reflected broad-scale shoaling of the thermocline (*23*) (Fig. 2D).

The CASA-VGPM model gave biospheric NPP estimates of 111 to 117 Pg C $year^{-1}$ for the September 1997 to August 2000 period (*24*). Using the same model and remote sensing data collected between 1978 and 1990, Field *et al.* (*9*) estimated biospheric NPP at 105 Pg C $year^{-1}$. Their estimate for the land component (56 Pg C $year^{-1}$) was about the same as that reported here. However, their estimate of ocean NPP (49 Pg C $year^{-1}$) was considerably lower than our results, largely because of higher C_{sat} values from SeaWiFS (1997–2000) than from CZCS (1978–86) (*9*, *25*).

Since September 1997, SeaWiFS has provided the first multiyear measurements of ocean plant biomass in over a decade, as well as the first single-sensor global observations of the photosynthetic biosphere. SeaWiFS NDVI and C_{sat} data provide a basis for quantifying temporal changes in NPP, which is a critical component of global carbon and nutrient cycles. Land and ocean productivity responds to changes in the physical environ-

ment across the temporal continuum of climate variability, with seasonal cycles dominating over interannual changes (Fig. 1). Our initial analysis of the first 3 years of SeaWiFS data suggests that this sensor will have the capacity to detect longer time scale, lower amplitude responses of the photosynthetic biosphere to climate change. Achieving this goal will require a long-term commitment to intercalibrated global observations and improved ε models (*26*) and remote sensing algorithms (*27*). As these developments are realized, the SeaWiFS record will provide a basis against which future estimates of Earth system elemental cycling can be compared.

References and Notes

1. R. B. Myneni, S. O. Los, C. J. Tucker, *Geophys. Res. Lett.* **23**, 729 (1995).
2. P. Maisongrande, A. Ruimy, G. Dedieu, B. Saugier, *Tellus* **47B**, 178 (1995).
3. R. B. Myneni, C. D. Keeling, C. J. Tucker, G. Asrar, R. R. Nemani, *Nature* **386**, 698 (1997).
4. C. J. Tucker, S. N. Nicholson, *Ambio* **28**, 587 (1999).
5. R. B. Myneni, C. J. Tucker, C. D. Keeling, G. Asrar, *J. Geophys. Res.* **103**, 6145 (1998).
6. The SeaWiFS sensor is mounted on the OrbView-2 spacecraft (*28*) and follows a sun-synchronous orbit with a noontime equatorial crossing. The sensor provides complete 4-km global coverage every 2 days. The mission has operationally produced oceanic, atmospheric, and terrestrial data products since September 1997. The complete SeaWiFS data set has been reprocessed three times to incorporate refinements in sensor calibration, atmospheric correction, and bio-optical algorithms. The present study uses data from the most recent, May 2000 reprocessing (*29*). Monthly lunar calibration images indicate a progressive decrease in sensitivity of <1% for the six visible wave bands and up to 10% for the near-infrared wave bands. By applying calibration corrections based on the lunar time series, temporal changes in radiometric sensitivity are corrected to within <1% (*29*, *30*).
7. SeaWiFS wave bands relevant for deriving C_{sat} values are 443, 490, 510, and 555 nm. The third reprocessing of SeaWiFS data used the OC4 chlorophyll algorithm (*29*). Comparison of OC4 modeled and 2849 in situ chlorophyll values indicated a correlation coefficient (r^2) of 0.892 and root mean squared (RMS) error of 0.222 (*29*). OC4 is a switching algorithm that calculates C_{sat} from the maximum value of the ratios: 443:555, 490:555, and 510:555. OC4 outperforms earlier single wave band ratio algorithms, such as OC2 (490:555), at the high and/or low end of naturally occurring chlorophyll concentrations (*29*). Comparison of SeaWiFS OC4-derived C_{sat} values and 103 coincident in situ measurements indicated an average difference between modeled and measured C_{sat} of <6% (RMS error = 0.301) for chlorophyll (Chl) concentrations between 0.029 and 6.42 mg m^{-3} (*29*). It is noteworthy that, between 0.07 and 5.0 mg Chl m^{-3} (i.e., 93% of the global ocean), OC4-based C_{sat} values are not substantially different than values derived from a single wave band ratio algorithm. Thus, the global-scale spatial and temporal patterns in C_{sat} and ocean NPP described here are not strongly dependent on the choice of C_{sat} algorithm.
8. For SeaWiFS NDVI data, cloud artifacts were reduced by applying a maximum 5 by 5 pixel spatial filter over evergreen broadleaf forest regions and a median 5 by 5 pixel spatial filter and a Fourier Adjustment over all other land surfaces (*31*, *32*). Missing data for needle leaf evergreen regions during winter at >45°N were estimated from October values. No statistically significant trends (95% confidence level) were introduced by these corrections. SeaWiFS NDVI data were calibrated with 1997–98 Advanced Very High-Resolution Radiometer (AVHRR) Fourier-adjusted, solar angle–corrected, interpolated, and reconstructed (FASIR) data (*32*) on a per biome basis to achieve compatibility with field NDVI and NPP data. Comparison of SeaWiFS and AVHRR NDVI data indicated a RMS error of 0.0037 for interannual variations. SeaWiFS exhibited no substantial orbital drift between September 1997 and August 2000. NDVI has, unlike some other vegetation indices, a consistent positive near-linear relation with the fraction of incident PAR absorbed by the vegetation canopy (FPAR) (*33*, *34*).
9. C. B. Field, M. J. Behrenfeld, J. T. Randerson, P. G. Falkowski, *Science* **28**, 237 (1998).
10. M. J. Behrenfeld, P. G. Falkowski, *Limnol. Oceanogr.* **42**, 1 (1997).
11. C. S. Potter *et al.*, *Global Biogeochem. Cycles* **7**, 811 (1993).
12. C. B. Field, J. T. Randerson, C. M. Malmstrom, *Remote Sens. Environ.* **51**, 74 (1995).
13. For the oceans, ε was modeled as a function of sea surface temperature (*10*). For land, the fraction of PAR absorbed by vegetation was calculated from NDVI (*32*), and ε was related to local variations in soil moisture and temperature. For the oceans, sea surface temperature fields were provided by coincident AVHRR measurements. Monthly, 9-km resolution PAR fields were obtained from five SeaWiFS visible wave bands with an algorithm adapted from Frouin and Chertock (*35*). For land, PAR was taken as the sum of direct and diffuse visible radiation from monthly maps provided by the National Centers for Environmental Prediction (NCEP) (*36*). Local soil moisture and temperature fields were obtained from NCEP monthly precipitation and 2-m air temperature maps.
14. M. J. McPhaden, *Science* **283**, 950 (1999).
15. Detecting temporal changes in NPP is critically dependent on the thorough characterization of drift in instrument sensitivity. Complete descriptions of SeaWiFS calibration and analysis methodologies have been published (*29*, *30*). Briefly, monthly lunar observations were used to check the stability of all SeaWiFS wave bands (*6*), and daily solar calibrations were used to verify the high-frequency stability of the sensor. Analyses of water-leaving radiances for the clearest ocean regions (Sargasso Sea, south Pacific near Easter Island, and the MOBY site near Hawaii) showed no temporal trend in any of the radiance fields for the 3-year SeaWiFS record. Likewise, the most densely vegetated land areas exhibited no temporal trend in NDVI. Analysis of NDVI values over the Sahara (i.e., lowest 2% of the NDVI spectrum) indicated a very slight increase over the 3-year time series, but this increase was smaller than the minimum quantization level (<0.004 NDVI units). Finally, global mean values for atmospheric parameters (e.g., optical thickness and angström exponent) exhibited no temporal trends. These results therefore indicate that lunar calibration corrections were highly accurate (*29*).
16. B. G. Mitchell, E. A. Brody, O. Holm-Hansen, J. Bishop, *Limnol. Oceanogr.* **36**, 1662 (1991).
17. C. W. Sullivan, K. R. Arrigo, C. R. McClain, J. C. Comiso, J. Firestone, *Science* **262**, 1832 (1993).
18. P. Boyd *et al.*, *Nature* **407**, 695 (2000).
19. NPP around 75°S approaches values observed at the same latitude in the Northern Hemisphere. Elevated NPP near the Antarctic continent likely reflects an influence of increased iron availability and water column stability associated with midsummer ice melt.
20. The potential increase in Southern Ocean NPP was calculated as the difference between Southern and Northern Hemisphere NPP at each degree of latitude multiplied by the area of open water at that latitude in the Southern Ocean.
21. F. P. Chavez *et al.*, *Science* **286**, 2126 (1999).
22. R. G. Murtugudde, S. R. Signorini, J. R. Christian, A. J. Busalacchi, C. R. McClain, *J. Geophys. Res.* **104**, 18351 (1999).
23. C. S. Meinen, M. J. McPhaden, *J. Clim.* **13**, 3551 (2000).
24. Only a fraction of the ENSO-scale change in NPP is sequestered into long-term storage pools, such as ocean sediments, soils, plant stems, and roots. The remaining carbon is respired as CO_2 back into the atmosphere within an annual cycle.
25. Ocean NPP estimates differ largely because of differences in ε models and input C_{sat} fields (*37*). We used the same ε model as Field *et al.* (*9*), which gave a mean global ε of 4.4 mg C (mg Chl)$^{-1}$ hour^{-1} for the SeaWiFS period and 4.6 mg C (mg Chl)$^{-1}$ hour^{-1} for the CZCS period, with similar seasonal patterns for both records ($r^2 = 0.77$). Our higher ocean NPP estimates are thus not due to changes in ε, but higher C_{sat} values. The reason that CZCS pigments (Chl a + pheophytin) are lower than SeaWiFS C_{sat} values is not yet certain. Likely explanations, all suggesting deficiencies with the CZCS data, are as follows: (i) Coverage: CZCS coverage was extremely nonuniform, such that the November 1978 to June 1986 composite still included large areas with only a few measurements. SeaWiFS provides global coverage every week. (ii) Calibration: The CZCS mission had no reliable onboard calibration or in situ observation program to monitor temporal changes in sensor performance, so calibration was based on assumed water-leaving radiances in low chlorophyll areas. SeaWiFS is an extensively calibrated instrument (*6*, *15*). (iii) Atmospheric correction: CZCS had only one near-infrared band (670 nm) for atmospheric aerosol corrections, and a constant angström exponent was assumed. SeaWiFS uses two bands (765 and 865 nm) and characterizes aerosol type on a pixel by pixel basis. (iv) Bio-optical algorithm: The CZCS pigment algorithm was based on 55 field measurements collected near the United States. The SeaWiFS C_{sat} algorithm is based on >2800 measurements from around the world (*7*).
26. Unexplained variance in ε is a source of uncertainty in all NPP estimates. For the oceans, ε is generally described as a function of surface temperature (*37*). To test the sensitivity of our ocean NPP estimates to ε, we recalculated NPP for the SeaWiFS record using the temperature-dependent model of Morel (*38*). Relative to our ε model (*10*), the Morel model yielded higher NPP values in the tropics and lower NPP at mid to high latitudes. Monthly mean global NPP was consistently higher by 0.3 ± 0.1 Pg C month^{-1} for the Morel model, but month-to-month variations in NPP for the two ε models were highly correlated ($r^2 = 0.82$). Consequently, the interannual changes in global NPP described herein would be little affected by this change in ε model.
27. NPP estimates reported here are based on globally parameterized remote sensing algorithms for NDVI and C_{sat} that can exhibit regional biases, such as in the Southern Ocean (*39*, *40*). Developing regionally tuned algorithms may thus improve future estimates of biospheric NPP.
28. S. B. Hooker, W. E. Esaias, *Eos* **74**, 241 (1993).
29. *NASA Technical Memorandum Ser. No. 2000-206892, Vols. 9–11* (NASA, Greenbelt, MD, 2000).
30. R. A. Barnes, R. E. Eplee, F. S. Patt, C. R. McClain, *Appl. Opt.* **38**, 4649 (1999).
31. P. J. Sellers *et al.*, *J. Clim.* **9**, 706 (1996).
32. S. O. Los *et al.*, *J. Hydromet.* **1**, 183 (2000).
33. P. J. Sellers, *Int. J. Remote Sens.* **6**, 1335 (1985).
34. J. M. Chen, *IEEE Geosci. Trans.* **34**, 1353 (1996).
35. R. Frouin, B. Chertock, *J. Appl. Meteorol.* **31**, 1056 (1992).
36. NCEP reanalysis data were provided by the NOAA-CIRES Climate Diagnostics Center, Boulder, CO, from their Web site at http://www.cdc.noaa.gov/.
37. M. J. Behrenfeld, P. G. Falkowski, *Limnol. Oceanogr.* **42**, 1479 (1997).
38. A. Morel, *Prog. Oceanogr.* **26**, 263 (1991).
39. H. M. Dierssen, R. C. Smith, *J. Geophys. Res.* **105**, 26301 (2000).
40. J. K. Moore *et al.*, *Geophys. Res. Lett.* **26**, 1465 (1999).

41. We thank members of the SeaWiFS Project Office and Orbimage Orbview-2 support staff for their diligent efforts in assuring the success of the SeaWiFS mission, NASA Headquarters for supporting the SeaWiFS project, B. Limketkai for technical assistance, and E. Stanley.

21 August 2000; accepted 12 February 2001